A New Strategy to Overcome Cycle Skipping: Frequency-Difference Waveform Inversion

Rehman Ali[*], Trevor Mitcham[*], and Nebojsa Duric[*]

[*]Department of Imaging Sciences, URMC, Rochester, NY, 14620 USA

ABSTRACT

Most ultrasound transducer designs are driven towards high frequencies by the need to maximize the resolution achievable by B-mode reflectivity imaging. Because full-waveform inversion (FWI) requires low frequencies to overcome cycle skipping, it is often difficult to apply FWI to the same high-frequency transducer hardware. Recent work on time-domain adaptive waveform inversion (AWI) addresses this based on a deconvolution approach to overcome cycle skipping. However, most clinical implementations of ultrasound tomography rely on frequency-domain FWI to quickly reconstruct images on clinically relevant time scales. Although the broadband nature of AWI makes it difficult to translate to the frequency domain, we can approximate the properties of AWI by using a frequency-differencing approach. We develop and describe both a model-domain and a data-domain method for frequency-differencing. Simulations and phantom experiments show that each frequency-differencing approach helps overcome cycle skipping by providing a sufficiently accurate starting model for FWI.

Keywords: Nonlinear inverse problems, waveform inversion, ultrasound, tomography

1. INTRODUCTION

Ultrasound tomography (UST) uses the transmission of ultrasound through tissue to reconstruct high-resolution images of tissue properties such as sound speed and attenuation. The most common clinical use of UST is breast imaging[1–4] where sound speed and attenuation serve as biomarkers for cancer detection. The full waveform inversion (FWI) algorithm responsible for high-resolution UST imaging relies on the accurate simulation of pressure fields in a heterogeneous medium. For the application to breast imaging, FWI often requires low-frequency signals (less than 1 MHz) to overcome cycle skipping caused by errors in a starting model. This is because FWI directly minimizes the error between simulated and measured signals. If the simulated signal is delayed or time-advanced by more than a half cycle relative to the measured signal, the underlying model used in the simulation will update in the wrong direction due to cycle skipping. Low frequencies lengthen this half-cycle window, allowing FWI to overcome errors in a starting model.[5] Unfortunately, the lack of low-frequency signal content on most ultrasound transducers currently designed for B-mode imaging prevents FWI from becoming more broadly applicable.

Adaptive waveform inversion (AWI) overcomes this dependence on low frequencies by modeling the mismatch between simulated and measured signals as a bank of impulse responses.[6] Rather than directly minimizing the error between simulated and measured signals, AWI drives these impulse responses toward zero-time lag, circumventing the cycle skipping problem. However, the main difficulty limiting AWI is its time-domain methodology as most clinical UST scanners rely on frequency-domain FWI for fast image reconstruction.[4,7] Fortunately, time lag is equivalent to a linear phase response in the frequency domain, so a frequency-domain implementation of AWI can be achieved by flattening this linear phase response. One way this can be achieved is by using a mathematical trick from sonar known as frequency-differencing.[8] By taking the ratio of signals at two different frequencies f_1 and f_2, we can produce a new signal at frequency difference $\Delta f = |f_1 - f_2|$. By minimizing the error between simulated and measured signals after frequency differencing, cycle skipping can be overcome by using a sufficiently small frequency difference Δf.

We briefly elaborate on the connection between AWI and this frequency differencing strategy. We also describe two approaches to frequency differencing: 1) a model-based approach that modifies FWI to simulate a

Further author information: (Send correspondence to Rehman Ali)
Rehman Ali: E-mail: rali8@stanford.edu

Medical Imaging 2024: Ultrasonic Imaging and Tomography, edited by Christian Boehm, Nick Bottenus, Proc. of SPIE Vol. 12932, 129320G · © 2024 SPIE · 1605-7422
doi: 10.1117/12.3006287

frequency-difference signal based simulations at frequencies f_1 and f_2, and 2) a data-driven approach where data is generated at frequency Δf via frequency differencing but is then passed through a standard FWI algorithm.

2. BACKGROUND

2.1 Frequency-Domain FWI Using the Helmholtz Equation

Using finite difference methods,[9] we solve the 2D Helmholtz equation to obtain a pressure field $\mathbf{u}$ for a given source δ, frequency $\omega = 2\pi f$, and slowness $\mathbf{s}$ (i.e., the reciprocal of sound speed):

$$(\nabla^2 + \omega^2 \mathbf{s}^2)\mathbf{u}(\omega, \mathbf{s}) = \delta(\omega), \tag{1}$$

After discretization, the $(\nabla^2 + \omega^2 \mathbf{s}^2)$ operator becomes a sparse matrix A that encodes the finite difference scheme so that equation (1) can be described using the following matrix-vector formulation (where $\mathbf{u}$ and δ are now vectors over spatial locations on the discretized grid):

$$A(\omega, \mathbf{s})\mathbf{u}(\omega, \mathbf{s}) = \delta(\omega), \tag{2}$$

Differentiating both sides of this equation with respect to s gives us:

$$\frac{\partial \mathbf{u}}{\partial \mathbf{s}} = -A^{-1}\frac{\partial A}{\partial \mathbf{s}}\mathbf{u} = -A^{-1}\frac{\partial A}{\partial \mathbf{s}}A^{-1}\delta, \tag{3}$$

Rather than observing the full pressure field $\mathbf{u}$ at all locations in space, we only observe the pressure field $\mathbf{p}$ at the ring array. The relationship between $\mathbf{p}$ and $\mathbf{u}$ is: $\mathbf{p} = K\mathbf{u}$, where K is a sampling operator that extracts the pressure field at each element of the ring array. The relationship between changes in slowness and changes in the simulated pressure field at the ring array is

$$\frac{\partial \mathbf{p}}{\partial \mathbf{s}} = -KA^{-1}\frac{\partial A}{\partial \mathbf{s}}\mathbf{u} = -KA^{-1}\frac{\partial A}{\partial \mathbf{s}}A^{-1}\delta, \tag{4}$$

The cost function for waveform inversion is:

$$E(\omega, \mathbf{s}) = \frac{1}{2}\sum_{i=1}^{N} \|\mathbf{p_i}(\omega, \mathbf{s}) - \mathbf{p_{obs,i}}(\omega)\|_2^2 = \frac{1}{2}\sum_{i=1}^{N} \left(\mathbf{p_i}(\omega, \mathbf{s}) - \mathbf{p_{obs,i}}(\omega)\right)^H \left(\mathbf{p_i}(\omega, \mathbf{s}) - \mathbf{p_{obs,i}}(\omega)\right), \tag{5}$$

where $\mathbf{p_i}$ and $\mathbf{p_{obs,i}}$ are the simulated and observed pressure measurements on the ring array for the i^{th} single-element transmission $\delta_\mathbf{i}$ (i ranges from 1 to N, the number of elements on the ring array). The gradient of $E(\omega, \mathbf{s})$ with respect to slowness $\mathbf{s}$ is given by:

$$\nabla_\mathbf{s} E = \sum_{i=1}^{N} Re\left\{\left(\frac{\partial \mathbf{p_i}}{\partial \mathbf{s}}\right)^H (\mathbf{p_i} - \mathbf{p_{obs,i}})\right\} = -\sum_{i=1}^{N} Re\left\{\left(\frac{\partial A}{\partial \mathbf{s}}\mathbf{u_i}\right)^H (A^H)^{-1}K^T (\mathbf{p_i} - \mathbf{p_{obs,i}})\right\}, \tag{6}$$

This definition of the gradient is used to implement the conjugate gradient method as done in prior work.[5,10]

2.2 Complex-Valued Source Scaling for Frequency-Domain FWI

The waveform inversion described in the previous section assumes that the correct phase and amplitude is used for each single-element source $\delta_\mathbf{i}$; however, in practice, the phase and amplitude of each source must be estimated from measured waveform. The following projection formula provides a complex scaling γ_i that accounts for both the amplitude and phase from each source i:

$$\gamma_i = \frac{\mathbf{p_i}^H \mathbf{p_{obs,i}}}{\mathbf{p_i}^H \mathbf{p_i}} \tag{7}$$

The source vector and pressure fields are scaled to $\{\delta_\mathbf{i} \to \gamma_i \delta_\mathbf{i}\}$, $\{\mathbf{u_i} \to \gamma_i \mathbf{u_i}\}$, and $\{\mathbf{p_i} \to \gamma_i \mathbf{p_i}\}$, respectively.

2.3 Understanding Time-Domain AWI in the Frequency Domain

As described in the introduction, AWI[6] computes the bank of Wiener filters (or impulse responses) $\mathbf{w_i}$ that converts measured data to simulated data. In the frequency domain, this deconvolution can be expressed as:

$$\mathbf{w_i}(\omega, \mathbf{s}) = \frac{\mathbf{p_i}(\omega, \mathbf{s})}{\mathbf{p_{obs,i}}(\omega, \mathbf{s})}. \tag{8}$$

Since $\mathbf{p_i}(\omega, \mathbf{s})$, $\mathbf{p_{obs,i}}.(\omega, \mathbf{s})$, and $\mathbf{w_i}(\omega, \mathbf{s})$ are all vectors, the division in equation (8) is performed element-wise. Additionally, to avoid division by zero, this division is regularized in practice:[11]

$$\mathbf{w_i}(\omega, \mathbf{s}) = \frac{\mathbf{p_i}(\omega, \mathbf{s}) \odot \mathbf{p^*_{obs,i}}(\omega, \mathbf{s})}{\mathbf{p_{obs,i}}(\omega, \mathbf{s}) \odot \mathbf{p^*_{obs,i}}(\omega, \mathbf{s}) + \epsilon^2}, \tag{9}$$

where $\odot$ refers to element-wise multiplication, the $*$ superscript refers to complex conjugation, and ϵ^2 is intended to be a small positive number that stabilizes the division-by-zero in this deconvolution. An inverse Fourier transform can then be used to compute the bank of impulse responses $\mathbf{w_i}(t, \mathbf{s})$ as a function of time t from the frequency responses $\mathbf{w_i}(\omega, \mathbf{s})$. The goal of AWI is to drive $\mathbf{w_i}(t, \mathbf{s})$ towards zero-lag delta functions. There are several ways to achieve this. If we isolate a single impulse response $w_{ik}(t, \mathbf{s})$ from $\mathbf{w_i}(t, \mathbf{s})$, where k would be an index over the receivers, the objective function used in AWI[6,11] would be:

$$f_{AWI}(\mathbf{s}) = \frac{1}{2} \sum_{i,k} \frac{\int_{-\infty}^{\infty} |T(t) w_{ik}(t, \mathbf{s})|^2 dt}{\int_{-\infty}^{\infty} |w_{ik}(t, \mathbf{s})|^2 dt} \approx \frac{1}{2} \sum_{i,j} \frac{\int_{-t_{trace}/2}^{t_{trace}/2} |T(t) w_{ik}(t, \mathbf{s})|^2 dt}{\int_{-t_{trace}/2}^{t_{trace}/2} |w_{ik}(t, \mathbf{s})|^2 dt}, \tag{10}$$

where $T(t)$ is a weighting function, and t_{trace} (replacing ∞) is the length of the signal traces. If $|T(t)|$ increases monotonically with $|t|$, the objective function must be minimized; conversely, if $|T(t)|$ decreases monotonically with $|t|$, the objective function must be maximized.

We first try to understand the case where the objective function would be minimized. If $T(t) = -jt$ where $j = \sqrt{-1}$, the Fourier transform of $T(t)w_{ik}(t, \mathbf{s})$ would be $\frac{dw_{ik}(\omega, \mathbf{s})}{d\omega}$. Therefore, by Parseval's Theorem, the objective function may be re-expressed in the frequency domain as

$$f_{AWI}(\mathbf{s}) = \frac{1}{2} \sum_{i,k} \frac{\int_{-\infty}^{\infty} \left| \frac{dw_{ik}(\omega, \mathbf{s})}{d\omega} \right|^2 d\omega}{\int_{-\infty}^{\infty} |w_{ik}(\omega, \mathbf{s})|^2 d\omega}. \tag{11}$$

Based on (11), it appears that the goal of AWI in the frequency domain is to minimize $\left| \frac{dw_{ik}(\omega, \mathbf{s})}{d\omega} \right|$ or flatten the frequency spectrum. Furthermore, this is consistent with driving $w_{ik}(t, \mathbf{s})$ towards a zero-lag delta function because the Fourier transform of a zero-lag delta function is a uniformly flat frequency spectrum.

In the prior work on AWI,[6] it is stated that FWI aims to drive $\mathbf{p_i}(\omega, \mathbf{s}) - \mathbf{p_{obs,i}}(\omega)$ towards $\mathbf{0}$ while AWI aims to drive the ratio $\mathbf{p_i}(\omega, \mathbf{s})/\mathbf{p_{obs,i}}(\omega)$ towards $\mathbf{1}$. However, based on our analysis above, we believe it is more accurate to say that AWI drives $\frac{d}{d\omega}(\mathbf{p_i}(\omega, \mathbf{s})/\mathbf{p_{obs,i}}(\omega))$ towards $\mathbf{0}$. In other words, if one were to choose frequencies ω_1 and ω_2 such that $\Delta\omega = \omega_2 - \omega_1$ is very small, then AWI can be thought of as driving $\mathbf{p_i}(\omega_1, \mathbf{s})/\mathbf{p_{obs,i}}(\omega_1)$ and $\mathbf{p_i}(\omega_2, \mathbf{s})/\mathbf{p_{obs,i}}(\omega_2)$ towards each other rather than towards $\mathbf{1}$ for all such choices of ω_1 and ω_2.

3. INNOVATION

Motivated by our frequency-domain analysis of AWI, we want to devise a frequency-domain waveform inversion scheme that drives

$$\frac{\mathbf{p_i}(\omega_2, \mathbf{s})}{\mathbf{p_{obs,i}}(\omega_2)} - \frac{\mathbf{p_i}(\omega_1, \mathbf{s})}{\mathbf{p_{obs,i}}(\omega_1)} \rightarrow \mathbf{0}. \tag{12}$$

Recall that AWI would apply to (12) for all ω_1 and ω_2 such that $\Delta\omega = \omega_2 - \omega_1$ is sufficiently small. However, we restrict ourselves in this work to using two frequencies at a time to minimize the cost of repeatedly solving the Helmholtz equation. Therefore, we multiply the expression (12) by $\frac{\mathbf{p_{obs,i}}(\omega_2)}{\mathbf{p_i}(\omega_1,\mathbf{s})}$ to obtain

$$\frac{\mathbf{p_i}(\omega_2,\mathbf{s})}{\mathbf{p_i}(\omega_1,\mathbf{s})} - \frac{\mathbf{p_{obs,i}}(\omega_2)}{\mathbf{p_{obs,i}}(\omega_1)} \rightarrow \mathbf{0}. \tag{13}$$

In other words, by forming the ratio $\bar{\mathbf{p}}_{\mathbf{obs,i}}(\omega_1,\omega_2) = \frac{\mathbf{p_{obs,i}}(\omega_2)}{\mathbf{p_{obs,i}}(\omega_1)}$ of observed data, we can form the corresponding ratio $\bar{\mathbf{p}}_{\mathbf{i}}(\omega_1,\omega_2,\mathbf{s}) = \frac{\mathbf{p_i}(\omega_2,\mathbf{s})}{\mathbf{p_i}(\omega_1,\mathbf{s})}$ of simulated data. The goal of a waveform inversion inversion algorithm under this frequency differencing scheme would be to drive $\bar{\mathbf{p}}_{\mathbf{i}}(\omega_1,\omega_2,\mathbf{s}) \rightarrow \bar{\mathbf{p}}_{\mathbf{obs,i}}(\omega_1,\omega_2)$. The transformation from (12) to (13) may seem like a simple juxtaposition of ratios but we find that waveform inversion based on (13) often converges more quickly to a more accurate solution, especially in this dual-frequency setup.

3.1 Model-Domain Frequency Differencing

The cost function for frequency-difference waveform inversion (FDWI) is

$$E(\omega_1,\omega_2,\mathbf{s}) = \frac{1}{2}\sum_{i=1}^{N} \|\bar{\mathbf{p}}_{\mathbf{i}}(\omega_1,\omega_2,\mathbf{s}) - \bar{\mathbf{p}}_{\mathbf{obs,i}}(\omega_1,\omega_2)\|_2^2\,. \tag{14}$$

However, the ratios $\bar{\mathbf{p}}_{\mathbf{i}}(\omega_1,\omega_2,\mathbf{s})$ and $\bar{\mathbf{p}}_{\mathbf{obs,i}}(\omega_1,\omega_2)$ need be regularized by ϵ^2 to avoid division by zero:

$$\bar{\mathbf{p}}_{\mathbf{obs,i}}(\omega_1,\omega_2) = \frac{\mathbf{p_{obs,i}}(\omega_2) \odot \mathbf{p}^*_{\mathbf{obs,i}}(\omega_1)}{\mathbf{p_{obs,i}}(\omega_1) \odot \mathbf{p}^*_{\mathbf{obs,i}}(\omega_1) + \epsilon^2}, \tag{15}$$

$$\bar{\mathbf{p}}_{\mathbf{i}}(\omega_1,\omega_2,\mathbf{s}) = \frac{\mathbf{p_i}(\omega_2,\mathbf{s}) \odot \mathbf{p}^*_{\mathbf{i}}(\omega_1,\mathbf{s})}{\mathbf{p_i}(\omega_1,\mathbf{s}) \odot \mathbf{p}^*_{\mathbf{i}}(\omega_1,\mathbf{s}) + \epsilon^2}. \tag{16}$$

The source scaling described in Section 2.2 is applied at both ω_1 and ω_2 to ensure the consistency of these ratios. The gradient of $E(\omega_1,\omega_2,\mathbf{s})$ with respect to slowness $\mathbf{s}$ is given by

$$\nabla_{\mathbf{s}} E = \sum_{i=1}^{N} Re\left\{\left(\frac{\partial \bar{\mathbf{p}}_{\mathbf{i}}}{\partial \mathbf{s}}\right)^H (\bar{\mathbf{p}}_{\mathbf{i}} - \bar{\mathbf{p}}_{\mathbf{obs,i}})\right\}, \tag{17}$$

where

$$\begin{aligned}\frac{\partial \bar{\mathbf{p}}_{\mathbf{i}}}{\partial \mathbf{s}} =& \left(\frac{\mathbf{p}^*_{\mathbf{i}}(\omega_1,\mathbf{s})}{\mathbf{p_i}(\omega_1,\mathbf{s}) \odot \mathbf{p}^*_{\mathbf{i}}(\omega_1,\mathbf{s}) + \epsilon^2}\right) \odot \frac{\partial \mathbf{p_i}(\omega_2,\mathbf{s})}{\partial \mathbf{s}} + \epsilon^2 \left(\frac{\mathbf{p_i}(\omega_2,\mathbf{s})}{\mathbf{p_i}(\omega_1,\mathbf{s}) \odot \mathbf{p}^*_{\mathbf{i}}(\omega_1,\mathbf{s}) + \epsilon^2}\right) \odot \frac{\partial \mathbf{p}^*_{\mathbf{i}}(\omega_1,\mathbf{s})}{\partial \mathbf{s}} \\ & - \mathbf{p_i}(\omega_2,\mathbf{s}) \odot \left(\frac{\mathbf{p}^*_{\mathbf{i}}(\omega_1,\mathbf{s})}{\mathbf{p_i}(\omega_1,\mathbf{s}) \odot \mathbf{p}^*_{\mathbf{i}}(\omega_1,\mathbf{s}) + \epsilon^2}\right)^2 \odot \frac{\partial \mathbf{p_i}(\omega_1,\mathbf{s})}{\partial \mathbf{s}}.\end{aligned} \tag{18}$$

This definition of the gradient was used to implement the conjugate gradient algorithm for FDWI.

3.2 Data-Domain Frequency Differencing

If we set $\omega_1 = \omega$ and $\omega_2 = \omega + \Delta\omega$, $\bar{\mathbf{p}}_{\mathbf{obs,i}}$ may be re-expressed in terms of ω and $\Delta\omega$ as

$$\bar{\mathbf{p}}_{\mathbf{obs,i}}(\omega,\Delta\omega) = \frac{\mathbf{p_{obs,i}}(\omega+\Delta\omega) \odot \mathbf{p}^*_{\mathbf{obs,i}}(\omega)}{\mathbf{p_{obs,i}}(\omega) \odot \mathbf{p}^*_{\mathbf{obs,i}}(\omega) + \epsilon^2}. \tag{19}$$

However, we would like to eliminate the dependence of $\bar{\mathbf{p}}_{\mathbf{obs,i}}$ on ω so that it solely depends on $\Delta\omega$. This is acheived by integrating both the numerator and denominator over ω in the frequency band $[\omega_{low},\omega_{high}]$:

$$\bar{\mathbf{p}}_{\mathbf{obs,i}}(\Delta\omega) = \frac{\int_{\omega_{low}}^{\omega_{high}} \mathbf{p_{obs,i}}(\omega+\Delta\omega) \odot \mathbf{p}^*_{\mathbf{obs,i}}(\omega) d\omega}{\epsilon^2 + \int_{\omega_{low}}^{\omega_{high}} \mathbf{p_{obs,i}}(\omega) \odot \mathbf{p}^*_{\mathbf{obs,i}}(\omega) d\omega}. \tag{20}$$

At this point, we can use the standard FWI algorithm with the following objective function:

$$E(\Delta\omega, \mathbf{s}) = \frac{1}{2}\sum_{i=1}^{N}\left\|\mathbf{p_i}(\Delta\omega, \mathbf{s}) - \bar{\mathbf{p}}_{\mathbf{obs,i}}(\Delta\omega)\right\|_2^2. \tag{21}$$

This objective function (21) is identical to the original FWI objective function (5), except that $\Delta\omega$ replaces ω and $\bar{\mathbf{p}}_{\mathbf{obs,i}}(\Delta\omega)$ replaces $\mathbf{p}_{\mathbf{obs,i}}(\omega)$. In other words, a single Helmholtz equation at frequency $\Delta\omega$ is used to simulate $\mathbf{p_i}(\Delta\omega, \mathbf{s})$; however, rather than compare $\mathbf{p_i}(\Delta\omega, \mathbf{s})$ to actual content $\mathbf{p}_{\mathbf{obs,i}}(\Delta\omega, \mathbf{s})$ at frequency $\Delta\omega$ (which may not be present with sufficient SNR in the recorded signal), we instead compare $\mathbf{p_i}(\Delta\omega, \mathbf{s})$ to $\bar{\mathbf{p}}_{\mathbf{obs,i}}(\Delta\omega)$ resulting from equation (20). The process used to generate $\bar{\mathbf{p}}_{\mathbf{obs,i}}(\Delta\omega)$ from existing data is very similar to what is used in frequency-difference beamforming[8] to overcome the same lack of low frequency content in existing signals.

As opposed to the previous section, where we modify FWI to precisely model the ratio of data at two different frequencies, here we focus on generating the data that can fit the existing FWI model. Of course, the process of generating $\bar{\mathbf{p}}_{\mathbf{obs,i}}(\Delta\omega)$ via equation (20) would not match the actual physics (i.e., diffraction) at frequency $\Delta\omega$, thereby introducing systematic discrepancies with the simulated results of the Helmholtz equation. Despite this limitation, we believe that data-domain frequency differencing may provide a more accurate starting model than ray tomography for initiating conventional FWI at a starting frequency with sufficient SNR.

4. METHODS

4.1 Starting Model Based on Frequency Differencing

Frequency-domain FWI is typically performed from the lowest possible frequency to the highest possible frequency to avoid cycle skipping while also reconstructing images at high resolution. Most often, FWI is limited in its ability to avoid cycle skipping due to the absence of low frequency data, ultimately requiring the use of more accurate starting models to overcome cycle skipping. In this work we consider frequency differencing as a starting model for FWI so that FWI can be started at a higher frequency. Model-domain and data-domain frequency differencing is used to initialize FWI. The result of each frequency differencing scheme, before and after FWI, is compared to FWI starting from a homogeneous starting model. To compare cycle skipping in each case, FWI is started at the same frequency.

4.2 Numerical Simulations

Figure 1(a) from our prior work[5] shows the ground-truth sound speed map for a numerical breast phantom derived from a contrast-enhanced cone-beam breast CT image in work from the Diagnostic Breast Center Göttingen (`https://doi.org/10.1016/j.tranon.2017.08.010`)[12] under the Creative Commons Attribution-NonCommercial-No Derivatives License (CC BY NC ND) (`https://creativecommons.org/licenses/by-nc-nd/4.0/`). A k-Wave simulation[13] with this numerical breast phantom was used to simulate 256 single-element transmissions with 2.5 MHz center frequency (75% fractional bandwidth) from a 11 cm diameter ring array with 256 elements. Received channel data (time traces for the received signal from each individual element for each single-element transmission) from these k-Wave simulations were used to reconstruct the sound speed using the algorithms described in Section 4.1. Noise was added to the received channel data simulated in k-Wave.

For the simulated data, each reconstruction begins with a 1515 m/s homogeneous model. The model-domain differencing uses several frequency pairs whose values range from 1.2 to 1.7 MHz with frequency differences ranging from 0.3 to 0.4 MHz. The data-domain differencing is used to construct frequency differences ranging from 0.3 to 1.25 MHz. For each choice of starting model (model-domain differencing, data-domain differencing, or homogeneous model), FWI starts at 1.2 MHz and ends at 1.7 MHz.

4.3 Phantom Experiments

Raw ultrasound channel data from a whole-breast UST system (Delphinus Medical Technologies Inc., Novi, MI) was used to reconstruct the speed of sound in a custom gelatin phantom with 8 circular inclusions of increasing diameter in a circular arrangement. The UST system consisted of a 22 cm diameter ring transducer with 1024 elements and a pulse center frequency of 2.5 MHz.

For this phantom dataset, each reconstruction began with a 1480 m/s homogeneous model. The model-domain differencing used several frequency pairs whose values range from 0.7 to 1.0 MHz with frequency differences ranging from 0.15 to 0.25 MHz. The data-domain differencing was used to construct frequency differences ranging from 0.05 to 0.5 MHz. For each choice of starting model (model-domain differencing, data-domain differencing, or homogeneous model), FWI started at 0.75 MHz and ended at 1.0 MHz.

In lieu of ground-truth values of the speed of sound in this phantom, we also perform FWI starting from 0.3 MHz (with a homogeneous starting model), which we assume to overcome cycle skipping and yield the true speed of sound in the phantom.

5. RESULTS AND DISCUSSION

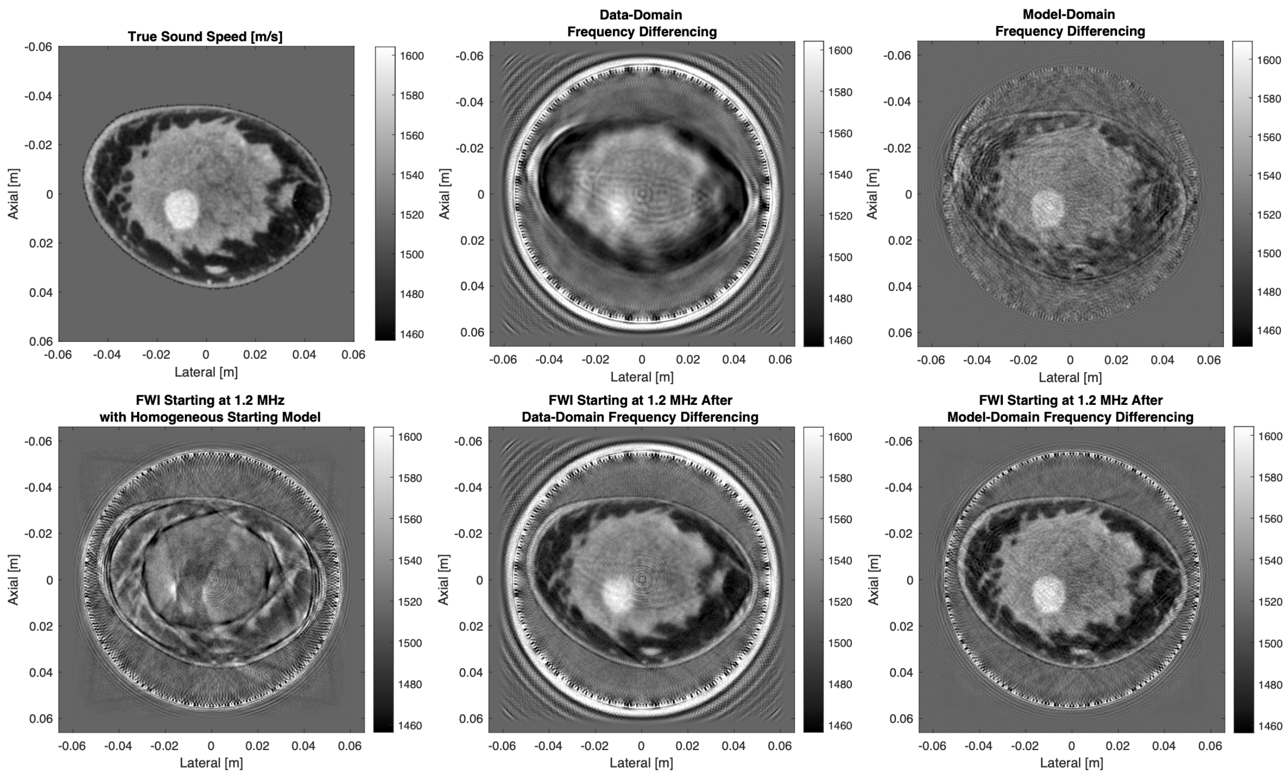

Figure 1. Demonstration of Frequency Differencing as a Starting Model for Conventional Frequency-Domain FWI in a Breast Imaging Simulation. In all reconstructions, no frequency content below 1.2 MHz was used; however, each frequency differencing method would be used to effectively synthesize frequency differences well below 1.2 MHz to overcome cycle skipping. Both data-domain and model-domain frequency differencing provide sufficiently accurate starting models for FWI to overcome the cycle skipping seen in FWI when starting from a homogeneous starting model.

Figure 1 shows the reconstruction of sound speed in a numerical breast phantom (true sound speed shown) based on data-domain and model-domain frequency differencing. When conventional frequency-domain FWI is started at 1.2 MHz from a homogeneous starting model, cycle skipping corrupts the entire image. When either frequency differencing method is used as the starting model for FWI, we can avoid cycle skipping even if FWI starts as high as 1.2 MHz. Qualitatively, data-domain and model-domain frequency differencing produce substantially different results. Data-domain frequency differencing appears to reconstruct a low-resolution but quantitative reconstruction of sound speed, reminiscent of ray tomography. On the other hand model-domain frequency differencing appears to reconstruct high-resolution features of the image while struggling to converge to exact quantitative values at all points in the image. This points out at least a few pros and cons of model-domain and data-domain frequency differencing.

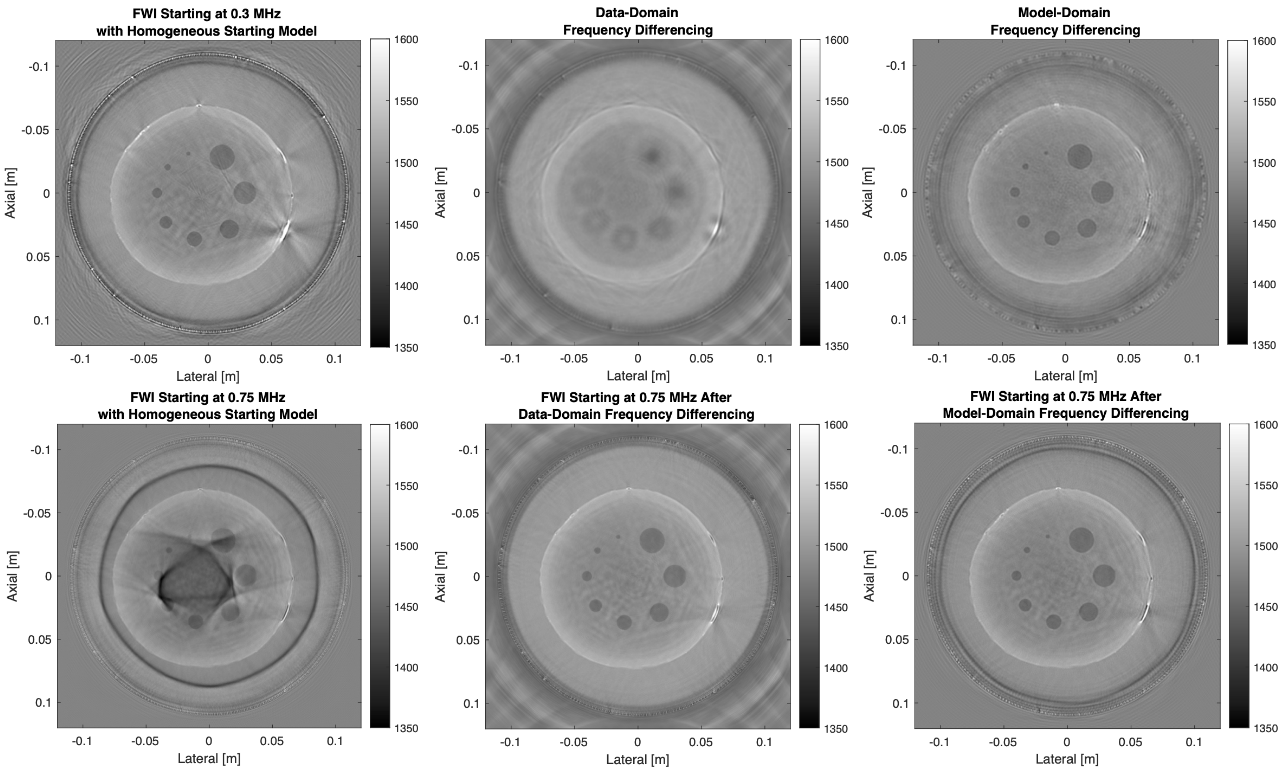

Figure 2. Demonstration of Frequency Differencing in Phantom Experiments. When FWI is started at 0.3 MHz from a homogeneous starting model, the phantom and all inclusion are clearly visualized without any cycle skipping. However, when the starting frequency is increased to 0.75 MHz, the reconstructed image is contaminated by cycle skipping. When either data-domain or model-domain frequency differencing is used as a starting model for FWI, FWI can now overcome cycle skipping at a starting frequency of 0.75 MHz. It is also interesting to note that model-domain frequency differencing substantially reconstructs the entire phantom prior to applying FWI.

The goal of data-domain frequency-differencing is to synthesize low-frequency information that is not present in the data. The process described by equation (20) introduces systematic error because it cannot accurately reproduce true content at this frequency. Therefore, this systematic error limits the imaging resolution of data-domain differencing in the same way that the inaccuracy of time-of-flight picks limits the resolution of ray tomography.[14,15] However, we generally reconstruct large-scale features accurately.

The goal of model-domain frequency differencing is to take two existing frequencies in the data, which would be subject to cycle skipping if FWI were applied to each frequency in isolation, and model their ratio to overcome cycle skipping. Although it may appear that accurately modeling this ratio would lead to a more accurate inversion while overcoming cycle skipping, the results shown in Figure 1 would indicate that this model may be poorly conditioned for inversion, especially in low signal-to-noise-ratio (SNR) conditions. One potential reason for this ill-conditioning is alluded by prior work on AWI,[6] which stipulates that AWI is a fundamentally finite-bandwidth concept that is unlikely to work on sparse-frequency data. It may be that more than a single ratio of two frequencies is necessary to overcome the issue of ill-conditioning. This raises the question of how many frequencies would need to be modeled without substantially increasing computational cost.

Figure 2 demonstrates both data-domain and model-domain frequency differencing in a phantom experiment and their impact on FWI as starting models. If FWI is started at 0.3 MHz, we can accurately reconstruct the phantom from a homogeneous starting model. However, FWI fails to reconstruct the phantom without cycle skipping when starting from 0.75 MHz when starting from the same homogeneous model. Both data-domain and model-domain frequency differencing provide sufficiently accurate starting models for FWI to overcome cycle skipping when starting from 0.75 MHz. It is also interesting to see that model-domain frequency differencing substantially reconstructs the entire phantom prior the application of FWI, which only introduces minor changes. Despite the concerns of low SNR in experiments, it may be that the ill-conditioning of the frequency-differencing model is not a signficant factor in this result because of the simplicity and low contrast of the phantom. Future work should examine these techniques in a variety of experimental conditions.

6. CONCLUSIONS

This work demonstrates both a model-domain and a data-domain frequency-differencing method to overcome cycle skipping when using FWI on data collected at high frequencies. These differencing methods essentially produce a difference frequency that is low enough to overcome the cycle skipping artifacts encountered during waveform inversion. Numerical and phantom experiments show that each frequency differencing method overcomes the cycle skipping encountered in FWI when using the same frequency content.

ACKNOWLEDGMENTS

This work was supported by the National Institute of Biomedical Imaging and Bioengineering (NIBIB) from the National Institute of Health (NIH) under grants F32-EB034589 and R01-EB028652.

REFERENCES

[1] Li, C., Duric, N., Littrup, P., and Huang, L., "In-vivo breast sound-speed imaging with ultrasound tomography," *Ultrasound in Medicine and Biology* **35**(10), 1615–1628 (2009).

[2] Duric, N., Littrup, P., Poulo, L., Babkin, A., Pevzner, R., Holsapple, E., Rama, O., and Glide, C., "Detection of breast cancer with ultrasound tomography: First results with the computed ultrasound risk evaluation (CURE) prototype," *Medical physics* **34**(2), 773–785 (2007).

[3] Schreiman, J., Gisvold, J., Greenleaf, J. F., and Bahn, R., "Ultrasound transmission computed tomography of the breast.," *Radiology* **150**(2), 523–530 (1984).

[4] Wiskin, J., Borup, D., Johnson, S., and Berggren, M., "Non-linear inverse scattering: high resolution quantitative breast tissue tomography," *The Journal of the Acoustical Society of America* **131**(5), 3802–3813 (2012).

[5] Ali, R., Mitcham, T., and Duric, N., "Impact of starting model on waveform inversion in ultrasound tomography," in [*Medical Imaging 2023: Ultrasonic Imaging and Tomography*], **12470**, 89–98, SPIE (2023).

[6] Warner, M. and Guasch, L., "Adaptive waveform inversion: Theory," *Geophysics* **81**(6), R429–R445 (2016).

[7] Sandhu, G., Li, C., Roy, O., Schmidt, S., and Duric, N., "Frequency domain ultrasound waveform tomography: breast imaging using a ring transducer," *Physics in Medicine & Biology* **60**(14), 5381 (2015).

[8] H. Abadi, S., Song, H., and R. Dowling, D., "Frequency-difference beamforming with sparse arrays," *The Journal of the Acoustical Society of America* **132**(3_Supplement), 2082–2082 (2012).

[9] Chen, Z., Cheng, D., Feng, W., and Wu, T., "An optimal 9-point finite difference scheme for the helmholtz equation with pml.," *International Journal of Numerical Analysis & Modeling* **10**(2) (2013).

[10] Ali, R., "Open-source full-waveform ultrasound computed tomography based on the angular spectrum method using linear arrays," in [*Medical Imaging 2022: Ultrasonic Imaging and Tomography*], **12038**, 187–205, SPIE (2022).

[11] Guasch, L., Warner, M., and Ravaut, C., "Adaptive waveform inversion: Practice," *Geophysics* **84**(3), R447–R461 (2019).

[12] Uhlig, J., Fischer, U., von Fintel, E., Stahnke, V., Perske, C., Lotz, J., and Wienbeck, S., "Contrast enhancement on cone-beam breast-ct for discrimination of breast cancer immunohistochemical subtypes," *Translational oncology* **10**(6), 904–910 (2017).

[13] Treeby, B. E. and Cox, B. T., "k-wave: Matlab toolbox for the simulation and reconstruction of photoacoustic wave fields," *Journal of biomedical optics* **15**(2), 021314 (2010).

[14] Li, C. and Duric, N., "Resolution limitation of travel time tomography: beyond the first fresnel zone," in [*Medical Imaging 2013: Ultrasonic Imaging, Tomography, and Therapy*], **8675**, 359–368, SPIE (2013).

[15] Ali, R., Hsieh, S., and Dahl, J., "Open-source gauss-newton-based methods for refraction-corrected ultrasound computed tomography," in [*Medical Imaging 2019: Ultrasonic Imaging and Tomography*], **10955**, 39–52, SPIE (2019).